Bioinspired Golden Spiral Shapes on Crushing Protection Behaviors of Tubular Structures

John Sherman, Wen Zhang, Hamza Waheed, Alexis Albarran, Hunter Crumpler, and Jun Xu*

Advanced structure design for energy absorption is a long-lasting pursuit due to its fascinating scientific merit in mechanics and important engineering application. Curves, a type of mathematical variation in geometry, are widely adopted in the biological system and biomaterial structures after long-time nature evolution toward optimization and adaption. Inspired by nature, a novel type of tubular structure is designed with golden spiral curvature. With the variations in the hierarchy of the supporting spirals and the number of arms, a maximum of 38.8% increase is demonstrated in performance over an uncurved counterpart structure. The computational modeling reveals that the additional added golden spiral arms within the tube enhance the rigidity and increase the energy dissipation via progress buckling involved by additional materials such that the energy absorption upon crushing is significantly improved. Theoretical models then provide intrinsic underlying mechanics analysis with more intuitive design guidance for such structures. Results develop an efficient yet simple design based on widely accepted tubular structure design for impact protection, enrich the mechanistic understanding of the nonlinear buckling behaviors, and provide applicable design guidance for engineering structures.

J. Sherman, W. Zhang, H. Waheed, A. Albarran, H. Crumpler, J. Xu
Department of Mechanical Engineering and Engineering Science
The University of North Carolina at Charlotte
Charlotte, NC 28223, USA
E-mail: jun.xu@uncc.edu

J. Sherman, J. Xu
Vehicle Energy & Safety Laboratory (VESL)
North Carolina Motorsports and Automotive Research Center
The University of North Carolina at Charlotte
Charlotte, NC 28223, USA

W. Zhang
Engineering Department
Nuro
Mountain View, CA 94043, USA

J. Xu
School of Data Science
The University of North Carolina at Charlotte
Charlotte, NC 28223, USA

The ORCID identification number(s) for the author(s) of this article can be found under https://doi.org/10.1002/adem.202300349.

1. Introduction

Impact protection and crashworthiness is a long-lasting research topic for engineering structure design due to the frequent occurrence of inevitable accidents. Traditionally, research has regarded natural materials,[1–4] whose structure may be developed evolutionarily as a response to environmental pressures, as a point of inspiration for designing structures that aid in structural safety design upon mechanical abusive loading. A traditional approach to best solving this problem is to take inspiration from nature, where evolutionary pressures yield promising results. Materials like bamboo,[5–8] fruit peel and nut shells,[9–11] carapaces of shrimp and crustaceans,[12–14] and wood, etc. have been investigated due to their superior strength and toughness. The mechanisms of the biomaterials and biosystems for lighter yet tougher structures mainly contain lightweight structure (hollow), geometry similarity (hierarchy), and material mismatch (mechanical behaviors).[15] Both geometry similarity and material mismatch may create a synergetic effect to promote the toughness of the structure to provide better impact protection.

In nature, highly efficient structures exhibit a self-similarity in their macro and microstructure, which optimizes packing space while improving structural rigidity alongside other factors. Similar geometries, often derived as hierarchy extensions of some baseline geometry, have been extensively investigated for their capabilities to improve cellular mechanical structures. Common techniques applied to investigate hierarchical design include membrane/corner alterations, variations of wall shape, and holistic unit cell alterations. One method is to apply supports at the membranes and corners,[16–18] which may then be extended in size,[7] geometry, or concentricity to provide a tailorable improvement in performance. The walls of the cellular structure may also be altered by creating layers of supportive material[19–21] or altering the local wall geometry.[22,23] An extensively investigated procedure supports the underutilized hollow region within the unit cell by either extending upon the existing geometry[16] of the structure or adding unrelated regions with potentially high-performing geometries.

The material mismatch is another powerful design strategy within the structures, which allows for additional resistance that self-similar structures cannot achieve. One common application is a variation of brick-and-mortar construction on composite

**ADVANCED
SCIENCE NEWS**

www.advancedsciencenews.com

**ADVANCED
ENGINEERING
MATERIALS**

www.aem-journal.com

materials[24,25] to allow for resistance to in-plane motion. Additionally, layering,[26] rotation,[12,14,27] and fibrous supports[24] show potential for the optimization of desired characteristics.

The most used energy absorption-efficient structures are bioinspired. An excellent example is the thin-walled tube.[28] Alterations to this humble structure show the great potential for future development in understanding optimal design in existing materials. Internal fillings can be added and varied,[29] such as gradient thickness inspired by the bone marrow,[29,30] bamboo-inspired topological supports, and fillings developed from metal materials. Corrugations have also shown improvements for both out-of-plane wall geometries, such as woodpecker beak[23] and horseshoe inspired, and in-plane variations like that of palm tree[31] and ribbed supports.[32,33] Additionally, tapering[34] has shown potential in allowing for the tailorability of such structures.

The golden spiral (GS) is a common structure in nature and design, often resulting from optimizing space filling, such as in sunflower seeds. Certain structural natural materials, like the shells of nautili, also utilize it. This structure has been mathematically simulated using the Fibonacci series to construct a procedural spiral. Although humans have traditionally mimicked this structure in architecture and art, its structural effects have been minimally studied. Given its predominance in shell-like structures, which must optimize between strength and weight, similar to the tortoise and beetle shells, investigating the mechanical properties of this structure could yield promising results.

Therefore, our natural idea is to propose a novel design combining a simple thin-walled tube with bioinspired GS serving as arms to gain improved energy absorption capability. Further, we also target to discover the new energy absorption mechanisms within such design via systematic mechanical characterization and computational and theoretical modeling. In Section 2, the design criteria and construction techniques for the spiral design are discussed. A modeling scheme is also presented alongside experimental techniques and model validation. Section 3 analyzes the results and investigates the underlying geometric influences. Additional considerations and computational frameworks are considered in Section 4, in which a theoretical methodology is derived. The effects of additional supports to mitigate the weakness of the structure are also investigated here. From this information, Section 5 concludes the discoveries herein and establishes principles for further investigation of the phenomena.

2. Experimental Section

2.1. Geometric Considerations

While many effects of geometry were measured by previous research, the curvature was mostly disregarded due to its high nonlinearity. We expected to implement such a complex mechanism using a curved arm to substitute a straight arm whose primary driving force in specific energy absorption (SEA) determination was its bending into a pseudocorner giving it effective membrane energy. This SEA criteria, which normalizes energy absorption against mass, is a common identifier in literature used to justify the effectiveness of certain structures at absorbing mechanical impact energy efficiently mean crushing force (MCF) or average crushing force during the plateau region of compression of the sample. To determine the efficacy of the pseudocorner, we designed a curved arm here as a central support structure to a traditional circular honeycomb unit cell.

Additional support was developed by progressively changing the rate of the curvature of the unit cell. While several methods existed for creating variant curvature, one common method was utilizing a spiral. A traditional spiral constructed in a series of circular portions was the GS, whose constructive radii for the larger quarter circular segments were developed from the Fibonacci series (**Figure 1**a).[35] A variation in the number of arms was also considered to understand how the spiral mechanisms compare to similar structures completely. Thus, we developed a GS unit cell whose spirals originated from the center of a tubular structure and radiated until they intersected with the tube. The hierarchy of the curvature, k, was created by adding additional quarter circles in the manner of creating a GS whose radii was calculated as $a_k = F_k \cdot a_0$, where a_k is the radius of the kth quarter circle, F_k is the kth Fibonacci number, and a_0 is the first k circle radius (Figure 1b). The number of arms is defined as the number of curvatures with the kth hierarchy (Figure 1c). Note that all the arms were evenly distributed along the circular tube.

2.2. Experimental Setups

Without loss of generality, we machined a representative tubular structure for two unit cell samples using wire electrical discharge
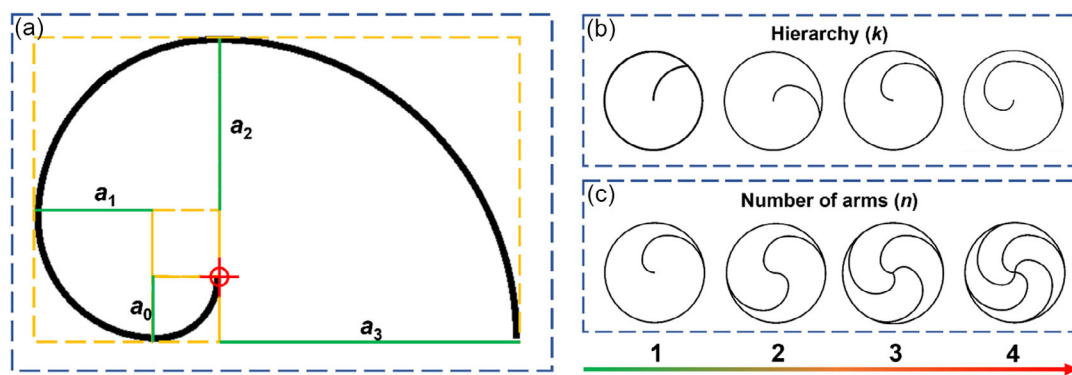

Figure 1. GS tubular structure design considering a) the spiral construction with a base unit a_0, b) the change in the hierarchy of the spiral (k), and c) the change in the number of structural arms (n).

ADVANCED
SCIENCE NEWS
www.advancedsciencenews.com

ADVANCED
ENGINEERING
MATERIALS
www.aem-journal.com

machining (WEDM) from 6061-t6 aluminum (**Figure 2**a). The samples had a thickness of $t = 0.5$ mm, height of $h = 60$ mm, and external radius $r = 15$ mm with $(n, k) = (2, 2)$. Each sample was weighed, measured, and placed into the SUNS universal material testing machine (300 kN maximum load). An in-plane orientation, where the geometries of the unit cells were planar with the compression platens, was utilized as the proposed structure was designed for such compression direction. A quasistatic displacement rate of 7 mm min^{-1} was applied to eliminate possible structural inertia effects.

2.3. Computational Model

To perform a variety of parametric studies, we established a finite-element (FE) model based on ABAQUS/Explicit with standard aluminum 6061-t6[36] with properties of density $\rho = 2700$ kg m^{-3}, Young's modulus $E = 69$ GPa, Poisson's ratio $\nu = .33$, and yield stress $\sigma_y = 270$ MPa with the plastic phase characterized by an elastic perfectly plastic material model. Due to the quasistatic deformation of the experiments, material strain rate dependency was disregarded for this model. In the meantime, for computational efficiency, the model utilized a quicker displacement to minimize the computation time without sacrificing the physics correctness. One key step here was to monitor the kinetic energy to ensure that the dynamic setup did not include inertial forces. The model was constrained by the top and bottom plates modeled as rigid bodies, with the bottom one fixed and the top given a constant displacement rate of 2 m s^{-1} to expedite the computational efficiency based on commonly accepted experience.[3] Note that the kinetic energy versus potential energy was monitored during run time to ensure that the relatively high velocity of the impacting plate would not introduce additional inertial effects. Normal and tangential penalty friction was given to the interface between the plates and the unit cell with a coefficient of friction of 0.2 to mimic the aluminum–steel interactions.[3] The unit cell was modeled using shell elements (S4R), with a mesh convergence of an optimal balance between accuracy and computational time, yielding element sizes of 1 mm.

3. Results

Experimental force–displacement curves for the $k = 2$ cells are compared to the model data. Both curves display the characteristic initial peak for the impactor force followed by an intense drop to a region of relatively stagnant force variation. The plateau of this structure remains stable until the force increases, and all potential buckling of the thin walls finalizes at ≈ 48 mm. At this point, the structure enters the densification region, and no more energy can be absorbed realistically by the structure. Deformation modes observed during experimental and model compressions in the plateau region show progressive buckling, which explains the peaks and valleys in this regime. This deformation mode is ideal for energy absorption materials in previous studies, as opposed to Euler buckling, where a global deformation of the structure results in reduced buckling that is utilized to absorb impact energy. To establish the validity of the FE model, the profiles of the model plateau regions were compared to the experimental results to ensure minimal variation. During this period, the MCF of both samples was found to be highly similar, with less than 5% variation (Figure 2b). Analyzing the profile of both samples during this regime, one may easily observe a nonsymmetrical collapse mode. The deformation profiles (Figure 2b) demonstrate similar progressive deformation modes by the comparison between experiment and computational results. Inspection of the final deformed sample shows similar collapse modes, with the central curved arms forming three distinct lobes. At the same time, the external tube mimics a diamond deformation mode (the deformation morphology may deviate, which is commonly seen in reported references). The model also exhibits a similar profile, with the only difference being the formation of the first lobe. This phenomenon may be attributed to the model boundary conditions being too ideal compared to the experiment. However, the final force–displacement curve shows minimal variation in the initial peak, where this phenomenon is present. Thus, the deviations can be reasonably ignored. Except for small fractures observed in the experimental sample, likely due to imperfections in the aluminum, which coincide with the lower peaks of the experimental force–displacement curve (the only
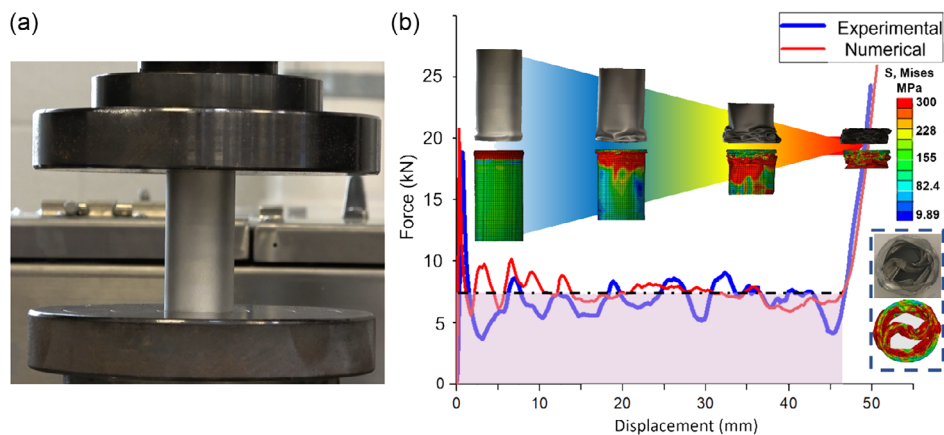

Figure 2. a) Experimental setup for quasistatic compression of $n = 2$, $k = 2$ model and b) force–displacement curves and profiles for experimental and numerical $n = 2$, $k = 2$ samples.

2300349 (3 of 10)

ADVANCED
SCIENCE NEWS
www.advancedsciencenews.com

ADVANCED
ENGINEERING
MATERIALS
www.aem-journal.com

clear points where the model deviates from the experiment), the model reasonably predicts the experimental performance of the structures. Hence, it can be further utilized to observe parametric variations in the structure.

The primary hierarchies focused on by this work are the n and k values. If we generalize the values starting from $n = 0$ and $k = 0$, we may end up with a traditional thin-walled tube (**Figure 3**). If $k = 0$ is fixed while n is varying, we create multiple straight arms within the thin-walled tubes. By gradually increasing the k value, we add more hierarchy (Figure 3a). For structures with $n = 1$, the free end of the arm located at the center is unconstrained, causing larger folds that minimize the supporting effects of the curvature. Additionally, higher k values result in longer arm sections with low curvature, which was previously regarded as ineffectual in SEA performance. Because of sporadic sectional attachment to the wall, the curves reduce their potential effects. One way to mitigate these effects is by providing supporting rings on the arms to constrain them to more ideal deformation modes (Figure 3b).

Supporting tubular rings were attached to the arms at the regions where the curvature changes in the GS to produce supported GS (S-GS) cells. In regions of changing curvature, it has been observed that the flattening of curves becomes less efficient. This is because existing lobes from lower hierarchies extend into lower-curvature areas instead of forming new lobes. As a result, the lower average curvature in these regions reduces the difficulty in inducing deformation, reducing the total available energy that can be absorbed. In addition to reducing the wasted deformations (**Figure 4**), this also controls the formation of lobes to be under a singular curvature, adding more lobes for an arm and reducing the effects of mixed curvature, creating more predictable and calculatable deformation mechanisms.

The higher n and k of GS showed the most consistent improvement over the canonical straight-supported cells;
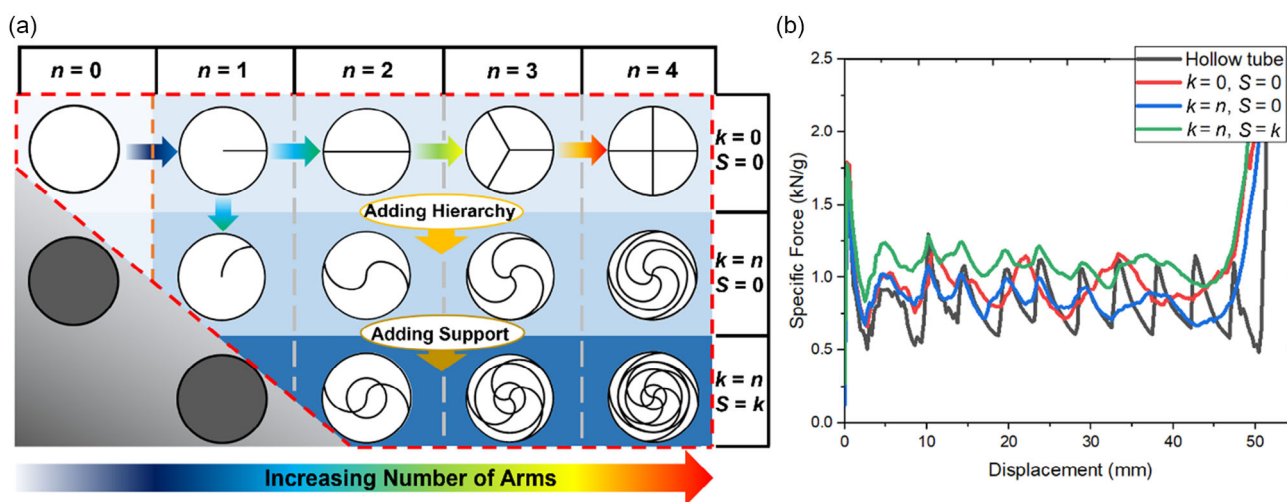

Figure 3. a) Construction methods for GS honeycombs considering n, k, and support criteria, and comparisons, and b) specific crushing force between each k hierarchy variation for an n = 2 tube.
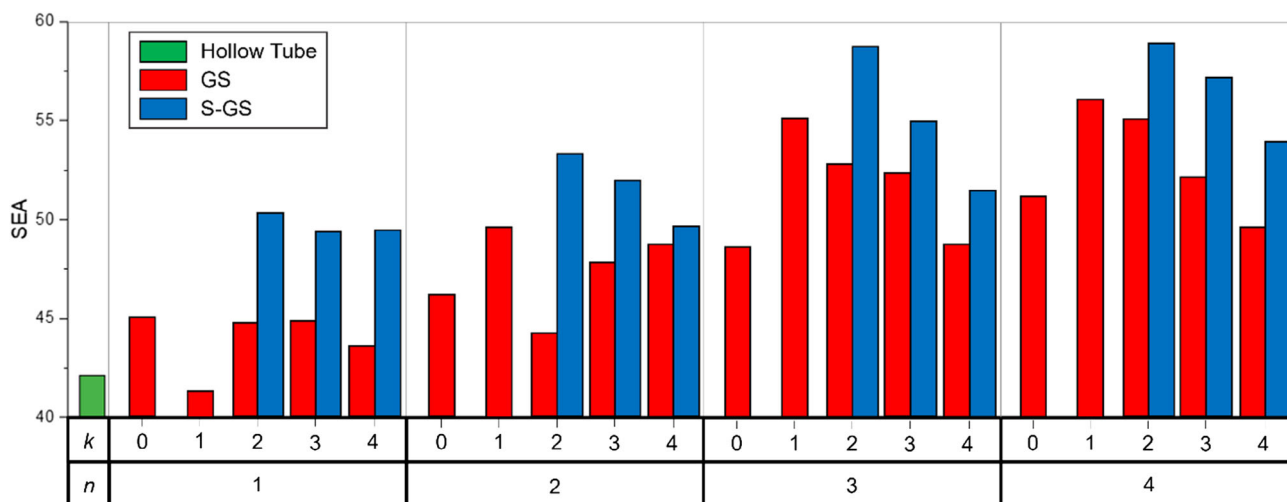

Figure 4. SEA results for numerical models of GS with n and k ranging from 1 to 4 compared against a traditional hollow circular tube.

however, it is not uniformly improving. By adding supports to the GS, the S-GS shows considerable and consistent improvement over the baseline tube, to a maximum 38.8% increase in SEA for a $k = 2$ $n = 2$ S-GS cell, the straight support, and the GS tube.

4. Discussion

4.1. Hierarchy

To create a complete understanding of the effects that the GS geometries curvature provides, k and n values are varied from 1 to 4 in FE models. In this section, to rule out the effect caused by the aspect ratio, we fix the $t/L = .067$. For cases with $n >= 5$, at this given t/L, we may observe Euler buckling for the structure.

To determine two major indicators for energy absorption evaluation, that is, MCF and SEA, the curves are analyzed as

$$\text{MCF} = \frac{\int_0^\delta F(x)\mathrm{d}x}{\delta} \tag{1}$$

$$\text{SEA} = \frac{\int_0^\delta F(x)\mathrm{d}x}{m} \tag{2}$$

with δ referring to the displacement after which densification occurs, and the energy being modified by a mass m, determined as[37]

$$\delta = \max\left(\frac{\int_0^x F(x)}{\max(F|_0^x)}\right) \tag{3}$$

or the last point at which energy absorbed by the sample outpaces the development of the maximum force until that point.

The parameters of both n and k increased MCF; however, a nonlinear relationship between SEA and MCF is noted by variant k values (**Table 1**). For a lower number of arms, the structural hierarchy of the k showed an increasing relationship with k values of 3 and 4 dominating the 2 hierarchy, but when presented with the complexity of the multipanel intersection between the arms as seen with n values above 2, the interaction at the conjunction point drives the lower hierarchies to become dominant. Interestingly, it is noted that when $k = 2$, the aforementioned pattern is broken by the $n = 2$ cell. This is due to the change in lobe sizes induced by the $n = 2$ elements, which alters the conditions for lobe creation at the end of the arms located in the center of the cell. For $k = 2$ cells, this modified lobe that is created is much less efficient at energy absorption than the ones developed for the other number of arms, while for all other k values this change in central lobe size has negligible detrimental effects on the response of the structure.

4.2. Variation of Structural Parameters

Given the limiting factor of cell size and thickness to choices of structural hierarchies, understanding how these factors play in the performance may allow for improvement of selection of n and k values and even allow for higher hierarchies. Consequently, models of the existing arm arrangements were run by parametrically changing the a_0 and t values (**Figure 4**).

In the meantime, the collapse mode of the structure is primarily dependent on the thickness, characteristic tube radius, and the number of arms (t, r_0, n) (**Figure 5**). To investigate these behaviors, a variable t/r_0 is developed from the parametric data, and the buckling modes are measured for all (n,k) cases. Two primary buckling modes are noted, that is, Euler buckling and progressive

Table 1. MCF and SEA for n and k values ranging from 1–4.

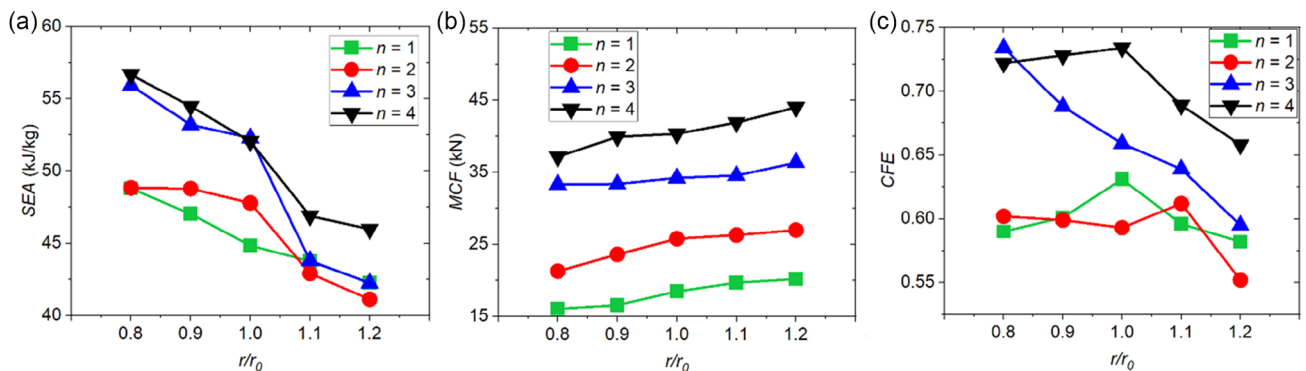| k	$n = 1$ MCF [kN]	$n = 1$ SEA [J g^{-1}]	$n = 2$ MCF [kN]	$n = 2$ SEA [J g^{-1}]	$n = 3$ MCF [kN]	$n = 3$ SEA [J g^{-1}]	$n = 4$ MCF [kN]	$n = 4$ SEA [J g^{-1}]
1	15.02	41.93	19.79	49.43	25.49	55.08	29.26	56.19
2	16.55	44.77	21.86	44.24	28.03	52.84	32.83	55.03
3	18.49	44.85	25.8	47.8	34.22	52.29	40.33	52.05
4	20.65	43.54	31.79	48.75	41.16	48.78	51.31	49.63

Figure 5. a) SEA, b) MCF, and c) CFE curves for a $k = 3$ GS unit cell with varying lengths (r/r_0) and number of arms n.

**ADVANCED
SCIENCE NEWS**

www.advancedsciencenews.com

**ADVANCED
ENGINEERING
MATERIALS**

www.aem-journal.com

deformation. Euler buckling dominates for high wall thicknesses, directing a transition of the plateau region to a progressive increase in force response. The red plane in the figure beginning at $t/r_0 = 0.05$ signifies the boundary of the green volume region, which contains progressive buckling mode. Despite the linear relationship between volume and k hierarchy in this region, there appears to be no dependence between buckling modes and k hierarchy.

The amount of support a cell structure provides depends on its k hierarchy. At low hierarchies, the outer tube attachments are angled to provide a supportive effect. However, at higher hierarchies, the angle becomes so shallow that the arms attach to the outer tube, and the curvature provides the largest resisting factor. This is evident in the strain energy profiles of the membranes. When investigating $n = 3$ samples for k values of 2 and 3, it was found that the $k = 2$ sample had a larger membrane effect from the intersection at the walls than the $k = 3$ sample, which treats the intersections as coincident. The region absorbing energy was noted to have uniform stress throughout the profile, but the strain varied throughout the walls and membranes. For the $k = 3$ models, the strain, and consequently the strain energy, was the same at the membranes as the outer ring, with only a 0.068% variation between elements taken at different sections. In contrast, the $k = 2$ model showed increased strain at the membranes, from an average of 0.073 at the outer ring to 0.131 at the membranes. This pattern was also observed throughout the curvature, with tighter curves having larger strains than those at the outer shell, leading to more energy dissipation through strain energy. In the $k = 3$ samples, the tube-arm membranes act similarly to the outer tube for energy absorption, making strain energy the predominant factor. As the variation of the spiral structure is the only parameter considered, all the improvements can be seen from the change in the spiral and not from any modifications to the outer tube. For samples with a low angle between the constructed arm and outer tube, that us, $k = 3$ $n = 3$, the benefit from the membrane and increased curvature, providing nodal strain energies of 0.734 and 0.926 J respectively, during the first peak in the plateau region, was seen to be lower than energies from lower hierarchies. Investigating the strain energy profiles throughout the wall for higher k cells, it is noticed that at the regions closer to the center, where the curvature is more extreme, the strain energy increases from 0.926 J on average to 1.972 J until the central membrane alters the profile. For lower k values, such as the $k = 2$ models, the peak energy in this region was lower, typically around 1.634 J. However, the distribution was more uniform, increasing the total average nodal energy absorbed. The presence of a central membrane stabilizes this effect. In contrast, for lower n models, the lack of a supporting membrane causes more unpredictable deformation modes, and this effect is less pronounced. This analysis demonstrates that solely increasing hierarchy may be ineffectual beyond a $k = 2$ threshold as the further increase in membrane energies did not outpace the increase in structure mass.

4.3. Theoretical Analysis

To better understand the driving mechanisms influencing MCF, and, consequently, SEA, a theoretical analysis of the plastic energies in the deformation modes is developed. To perform this a traditional analysis is performed on individual cases for constitutive elements and the resulting predicted responses are summed as membrane energies which must be absorbed during compression. Two primary constitutive elements are of focus, the connections between the rounded arms and circular tube (Type I) and the rounded panels (Type II) (**Figure 6**a). If n is greater than 2, a second element of type I becomes present, which consists of an even spacing of plates intersecting in the center. In the other scenarios, Type I is dominated by $n = 3$ membrane intersections whose angle of intersection is variant on the k value. The curvature effects of Type II elements are well studied.[38] However, considering the construction method of the arms, a singular series of equation does not exist for their deformation and must be derived. This is due to a transition of the hinge angle (**Figure 7**) which requires a discrete solution to be derived. The plateau deformation can be defined by a known energy analysis along a wavelength $2H$ for each element. The material can be described by a rigid-perfect plastic model from its thin wall deformation modes, and a complete understanding of the energies can be conducted from a summation of the membrane and bending energies developed from the energy analysis.

Type 1: Out-of-plane compression of the membranes

To determine a theoretical framework

$$2\kappa PH = W_B + W_M \tag{4}$$

where W_B refers to the requisite bending energy and W_M refers to the energy required to deform rigid membranes. As the entire wavelength cannot be utilized due to a bending radius at the hinge, a modifying value κ typically found to be 0.7–0.75[39] is utilized. Here, it is found as 0.73. The bending energy is proportional to the total wall length of the body and is found as
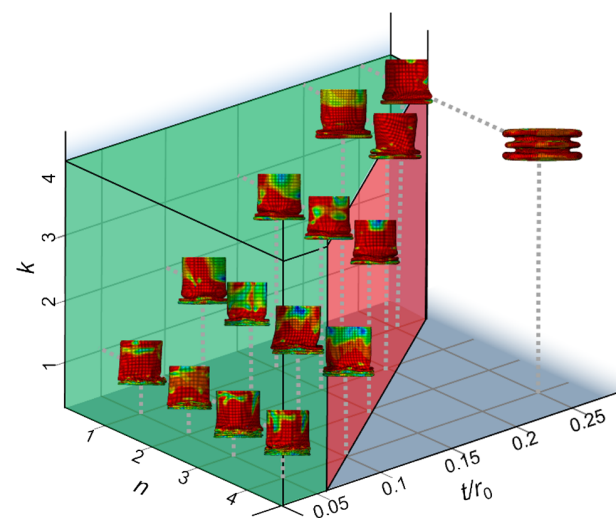
$$W_B 2\pi M_0 L \tag{5}$$

Figure 6. a) Visualizations of the membranes for a $n = 3$, $k = 3$ sample, and b)the transformation of hinge lines due to curvature from a hollow tube to a constructed spiral curvature.
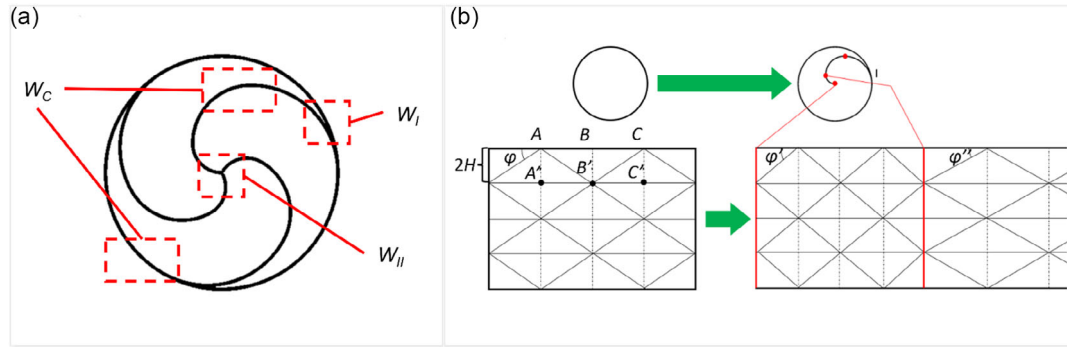
Figure 7. Regions of Euler and progressive (green) buckling for GS dependent on k, n, and t/r_0.

with M_0 being the plastic bending moment defined as $\sigma_0 t^2/4$ with the flow stress σ_0 being $\sqrt{\sigma_y \sigma_u/(1+\gamma)}$ for an ultimate strength σ_u of 300 MPa and strain hardening exponent γ found to be 0.04.[36]

There are three membranes found in the model, that is, the angled connection of the arms to the wall W_I, the connection of the arms for the case $n > 2$ W_{II}, and the pseudo membrane W_C created by the curvature. The three-panel membrane can be derived from the three-panel element theory.[7,40] To determine the coincident angle, the curved elements must first be viewed as straight. From this assumption, the radius of the outer tube can be measured against the constructed a_k radius from the kth quarter circle to determine a corresponding γ to use as the central panels angle. The panel and thickening membranes adjusted for one wavelength can be respectively denoted by

$$W_p = \frac{4}{t} H^2 M_0 \tan\left(\frac{\gamma}{2}\right) + \frac{2}{t} H^2 M_0 \sin(\gamma) \tag{6}$$

$$W_t = \frac{6}{t} H^2 M_0 \sin(\gamma) \tag{7}$$

due to the 180º connection between the side panels. When compiled, this results in complete membrane energy of

$$W_I = W_p + W_t = \frac{4}{t} H^2 M_0 \tan\left(\frac{\gamma}{2}\right) + \frac{8}{t} H^2 M_0 \sin(\gamma) \tag{8}$$

While this theory adequately describes the three-panel interactions, a γ smaller than 30° has been noted to cause the panels to collapse onto each other, making accurate theoretical analysis of these membranes more difficult. For this study, these effects are seen to have minimal impact on the three-panel theory, so they have not been considered.

Additionally, the n-cross intersection may be determined from the n-cross theory developed by[41] as

$$W_{II} = \frac{4}{t} H^2 M_0 \tan\left(\frac{\pi}{2} - \frac{\pi}{n}\right) \tag{9}$$

While these membranes take effect in most models, W_I is disregarded from the $k=3$ morphology as the coincident angle

becomes 0, making the γ approximation invalid in accordance with the three-panel element theory.

Type 2: Out-of-plane compression of the curved panels

Given the difficulties concerning deformations of curved panels, an analysis based on ref. [38] is conducted. The construction of the arms is based on quarter circular elements, the analysis will be performed as if the arms were circular with modifications considering the variation in lobe length induced by curvature changes. However, the interaction between regions of differing curvature where the construction radius changes discretely leads to uncertainties in hinge line formation and rolling radius determination.

The collapse of the unit cells was noted as nonsymmetric, defined as a variation in the number of lobes on a compressed surface N. For most tubes, this can be seen as varying from two to five, with circular tubes with t/L ratios similar to the ones proposed in this paper possessing $N = 3$.[42] However, this is not a reasonable case for the arms and must be adjusted for the outer wall considering the effects the membranes interaction have on changing the number of lobes on multicell tubes. As the arm wall interactions induce a nucleation mechanism for the formation of different lobes, a multicell deformation based on the development of diamond lobes is considered opposed to a standard circular tube theory. The deformation for curved structures by a progressive diamond mode is traditionally defined by work dissipated along the arrangement of triangular subsections, such as flattening of the curved sections (W_{III}), bending around the inclined hinges (W_{IV}) and the horizontal hinges (W_V), and the axial travel of such hinges. To determine the complete crushing of the pseudomembrane W_C, the membranes W_{III}, W_{IV}, and W_V are calculated independently and summed.

The flattening of the curves[5] is denoted by

$$W_{III} = 2 \frac{L}{r} M_0 H \tag{10}$$

The bending at the inclined hinges can be measured by finding the lengths of the hinge lines AB', BC,' etc. For a circular tube 2 N, inclined hinges can be found and utilizing the assumption of the hinge angles $\varphi = \pi/2N$ an individual hinge length of $\frac{\pi D}{\cos\varphi}$ may be found. This hinge angle does not hold for the arm elements as $\varphi \to \varphi'$ (Figure 5), leading to an uncertain number of lobes for the completed structure. This phenomenon is due to

2300349 (7 of 10)

the nature of the folding wavelength $2H$ being kept constant for all portions of the curve, meaning certain sections will have divergent hinge angles from the predicted φ. It was assumed that the tube wavelength stayed constant regardless of arm curvature leading to the previous determination of the hinge angle being true for the external tube but failing due to the hinge angle transition for the arms.

Additionally, the free end for $n = 1$ scenarios complicates the analysis as the unrestrained condition allows for unpredictable bending, which is generally found to dissipate energy poorly. To approximate the development of lobes, the deformation modes of the models and experiments were compared to confirm the apparent number and size of the models for similarity check. We may clearly see that after enough hierarchy is developed, the location of certain hinges stays stagnant while emerging hinges migrate until a decisive distance is found. It could be assumed a similar lobe length to radius ratio as that of a circular tube. However, the arms are constructed on quarter circle segments and cannot be neatly divided into the previously defined hinge angle nor does it consider the apparent mixing of differing radii quarter circles in lobes. Based on observation, a compromise is made to determine a stable lobe length of $\beta_0 = 2\pi\alpha_0$ and for regions that would intersect a membrane $\beta' = \pi\alpha_0$. If the scenario above could not be met for all lobes along the arm, β' will be satisfied first, followed by each characteristic lobe length β_i such that no lobe will be longer than β_0 and all subsequent lobe lengths are equivalent with maximum length β_0. The angles at defining the lengths could then satisfy the relationship

$$\varphi_i = \tan^{-1}\left(\frac{L\tan(\varphi)}{\beta_i}\right) \tag{11}$$

for a lobe length L of the outer tube. As such, the hinge length becomes $\frac{\pi D}{\cos \varphi'}$ leading to membrane energy of

$$W_{IV,i} = \frac{M_0\pi\beta_i}{\cos(\varphi_i)} \tag{12}$$

The bending of the horizontal hinges remains a simple prospect of extrapolating the bending energy for the horizontal hinges of a tube and changing the characteristic length to that of the tube with the arms becoming

$$W_V = 2\pi M_0 L \tag{13}$$

This value is already considered in the bending energy formulation.

Deformation throughout the length of $2H$ is not continuous but evolves with the migration of a traveling hinge. This hinge progressively transformed the curved surfaces into a flat plane along a rotation of $2\,H\,r^{-1}$. The total work can be measured from this as $4\pi M_0\lambda H/r$ with r being found from $OA - \frac{D}{2}$.[5] OA refers to the outer region of the undeformed body, which for the arms is dependent on φ', and the diameter D is undeformed initial diameter. As certain lobes may share two differing radial elements, D for these segments can be found as an average of these values. The resulting rolling radius can be found as

$$r = \frac{a\pi - b\sin(2\varphi_i)}{c\sin(2\varphi_i)} \tag{14}$$

where a, b, and c are determined by the k hierarchy and the lobe length. The finalized work done at the rolling radius may be determined as

$$W_{V,i} = 4M_0\frac{H\beta_i}{a_0}\frac{c\sin(2\varphi_i)}{a\pi - b\sin(2\varphi_i)} \tag{15}$$

Such energy must be summed for each individualized lobe, which leads to long functions for certain k values. It can be noted that three-membrane forms may be found from Equation (4), that is, 1) those proportional to H^2 and comprise curvature and multipanel membrane effects; 2) those proportional to H^1 which are only found because of the curvature; and 3) those proportional to H^0 or the bending energy. By considering this, Equation (4) may be rewritten as

$$2\kappa PH = W_B + \overline{W}_1 H + \overline{W}_2 H^2 \tag{16}$$

By utilization of the stationary condition

$$\frac{\partial P}{\partial H} = 0 \tag{17}$$

the half wavelength H may be determined to be

$$H = \sqrt{\frac{W_B}{\overline{W}_2}} \tag{18}$$

The calculated theoretical values can be seen in **Figure 8**b. Practically, when applied to a unit cell of $(k,n) = (2,2)$, the P may be found as

$$P = \sigma_0(13.67\sqrt{rt^3} + 21.41t^2) \tag{19}$$

Additionally, note that for higher k values, the segment defined as the last lobe would occasionally attach itself to the outer wall rather than conduct itself as part of its own buckling deformation. This is likely due to the shallow angles of the higher hierarchies and the relatively low curvature for the external sections of the arms with respect to the external tube, requiring less energy to match the deformation of the tubular sections. This phenomenon would alter the membrane energy at the intersections of the arms and tubes, changing total SEA. Such interactions would happen only in certain cases, and it would be inaccurate to assume that the membrane energies can be neglected for higher hierarchies. However, it plays a factor in the divergence between the numerical and theoretical values. A modified three-panel membrane equation that considers the collapse of the panel for shallow γ may help improve the theoretical equations for high k values.

A theoretical effect of the curvature can then be derived by assuming a reasonably invariant densification deformation Δ and an approximated mass determined as $m = \rho h\lambda t$ with a total wall length of λ. By analysis, Δ varies from 45 to 50 mm which is a low enough variation to disregard its effects when considering the magnitude of the other variables. From this SEA may be theoretically found as
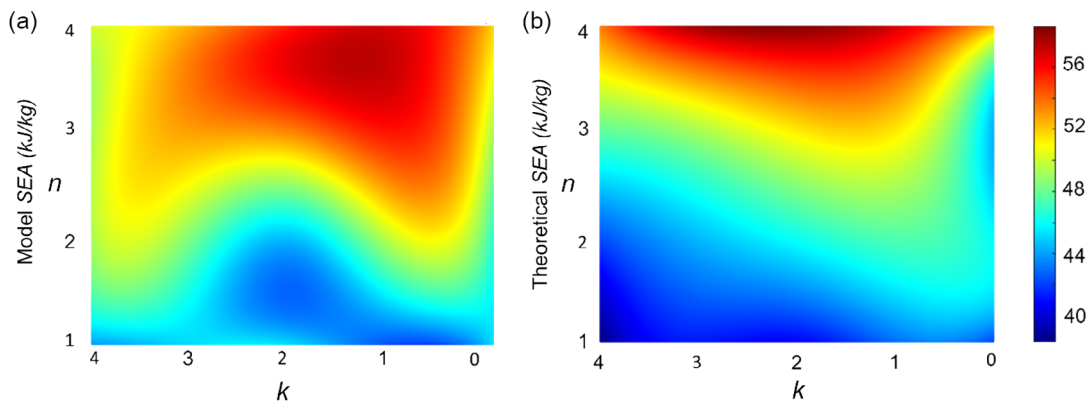
Figure 8. Surface plot of SEA versus number of arms and hierarchy for a) Numerical model data and b) Theoretical analysis.

$$\text{SEA} \propto \left(A\sqrt{\frac{t}{r}} + B\frac{t}{r} \right) \quad (20)$$

where A and B are modified considering k and n parameters. Equation (19) clearly demonstrates that the variant factors become solely λ and t. As curvature increases, the total length also increases, and the resultant bending energies adjust accordingly. Therefore, an increase in length has a detrimental effect on SEA for any generalized structure, which it must overcome with membranes. This explains, in part, the tendency for smaller tubes to outperform their larger counterparts until they become buckling dominant regarding SEA. For such curved structures to be worth further investigation, the improvements of the curvature must outpace the detriments derived from the increase in total wall length.

5. Conclusion

A novel bioinspired, simple, yet efficient structure was proposed. We note that currently, there is no available cost-effective large-scale manufacturing way for such complicated geometry; however, we believe this opens a new design perspective for innovative structural designs for possible applications in non-cost-sensitive and small-volume settings. The fundamental mechanism for the enhanced energy absorption capability upon crushing was revealed. The influence of curvature on the mechanical performance of energy absorbers was investigated by designing and modeling tubes with GSs used as support structures. The computational models were validated by experimental data and were used to produce a series of parametric data to determine the scope of performance of such structures. In certain situations, we witnessed notable improvement from the GS structures to their straight counterparts. For samples with a low angle between the constructed arm and outer tube, the benefit from the membrane and increased curvature was seen to be lower than expected as the increase in membrane energies did not outpace the increase in structure mass. Consequently we proposed S-GS models to further enhance the structure design and noted considerable improvement. By inducing a more desirable hinge length and creating membranes with less obtuse angles, the supported models mitigated the problems

with progressive curvature in the GS structure. The model data and insights from theoretical inspection show points of interest for improving the performance of traditionally underutilized straight segments. Predominantly, if the curvature of the curved sections is sufficiently small, a considerable increase in performance can be noticed, but as curvature increases, the effect becomes negligible and unstable. Results provide new concepts for structural design upon mechanical abusive loading and enrich the knowledge regarding the energy absorption behaviors for curved panels/sheets.

Conflict of Interest

The authors declare no conflict of interest.

Data Availability Statement

The data that support the findings of this study are available from the corresponding author upon reasonable request.

[1] N. Sac, G. Lu, *Composites, Part B* **2020**, *181*, 107496.
[2] B. S. Lazarus, A. Velasco-Hogan, T. Gómez-del Río, M. A. Meyers, I. Jasiuk, *J. Mater. Res. Technol.* **2020**, *9*, 15705.
[3] J. Sherman, W. Zhang, J. Xu, *Acta Mech. Solida Sin.* **2021**, *34*, 884.
[4] H. Gao, *Int. J. Fract.* **2006**, *138*, 101.
[5] D. Hu, Y. Wang, B. Song, L. Dang, Z. Zhang, *Composites, Part B* **2019**, *162*, 21.

[6] T. Tan, N. Rahbar, S. M. Allameh, S. Kwofie, D. Dissmore, K. Ghavami, W. O. Soboyejo, *Acta Biomater.* **2011**, *7*, 3796.

[7] W. Zhang, T. X. Yu, J. Xu, *Extreme Mech. Lett.* **2022**, *52*, 101640.

[8] J. Fu, Q. Liu, K. Liufu, Y. Deng, J. Fang, Q. Li, *Thin-Walled Struct.* **2019**, *135*, 400.

[9] W. Zhang, S. Yin, *Int. J. Impact Eng.* **2019**, *125*, 163.

[10] B. Gludovatz, F. Walsh, E. A. Zimmermann, S. E. Naleway, R. O. Ritchie, J. J. Kruzic, *J. Mech. Behav. Biomed. Mater.* **2017**, *76*, 76.

[11] N. Xiao, M. Felhofer, S. J. Antreich, J. C. Huss, K. Mayer, A. Singh, P. Bock, N. Gierlinger, *R. Soc. Open Sci.* **2021**, *8*, 210399.

[12] D. Ginzburg, F. Pinto, O. Iervolino, M. Meo, *Compos. Struct.* **2017**, *161*, 187.

[13] S. Kamat, H. Kessler, R. Ballarini, M. Nassirou, A. H. Heuera, *Acta Mater.* **2004**, *8*, 2395.

[14] S. Yin, H. Chen, R. Yang, Q. He, D. Chen, L. Ye, Y. W. Mai, J. Xu, R. O. Ritchie, *Cell Rep. Phys. Sci.* **2020**, *1*, 100109.

[15] W. Zhang, T. X. Yu, J. Xu, *Eng. Struct.* **2022**, *265*, 114490.

[16] Y. Zhang, X. Xu, J. Wang, T. Chen, C. H. Wang, *Int. J. Mech. Sci.* **2018**, *140*, 407.

[17] Q. Chen, Q. Shi, S. Signetti, F. Sun, Z. Li, F. Zhu, S. He, N. Pugno, *Int. J. Mech. Sci.* **2016**, *111–112*, 125.

[18] G. Sun, H. Jiang, J. Fang, G. Li, Q. Li, *Mater. Des.* **2016**, *110*, 705.

[19] H. Yin, X. Huang, F. Scarpa, G. Wen, Y. Chen, C. Zhang, *Compos. Struct.* **2018**, *192*, 516.

[20] J. Qiao, C. Chen, *Int. J. Solids Struct.* **2016**, *85–86*, 57.

[21] Y. Chen, Z. Jia, L. Wang, *Compos. Struct.* **2016**, *152*, 395.

[22] X. Yang, Y. Yao, J. Yang, Q. Pan, *Thin-Walled Struct.* **2018**, *125*, 1.

[23] N. S. Ha, G. Lu, X. Xiang, *J. Mater. Sci.* **2019**, *54*, 6286.

[24] H. H. Tsang, S. Raza, *Compos. Struct.* **2018**, *195*, 199.

[25] P. Tran, T. D. Dgo, P. Mendis, *Comput. Mater. Sci.* **2014**, *82*, 134.

[26] L. Burns, A. P. Mouritz, D. Pook, S. Feih, *Composites, Part B* **2015**, *69*, 222.

[27] S. Yin, R. Yang, Y. Huang, W. Guo, D. Chen, W. Zhang, M. Ren, Y. Zhou, J. Xu, *Compos. Sci. Technol.* **2021**, *205*, 108650.

[28] D. Zhang, G. Lu, D. Ruan, Q. Fei, *Int. J. Mech. Sci.* **2020**, *171*, 105403.

[29] Y. Li, Z. Fan, S. Hu, F. Zhang, L. Hu, Z. Xue, *Thin-Walled Struct.* **2022**, *178*, 109449.

[30] C. Wang, Y. Li, W. Zhao, S. Zou, G. Zhou, Y. Wang, *Int. J. Mech. Sci.* **2018**, *138–139*, 489.

[31] N. S. Ha, G. Lu, X. Xiang, *Int. J. Mech. Sci.* **2018**, *148*, 409.

[32] A. Amhadi, M. Asgardi, *Proc. Inst. Mech. Eng., Part C: J. Mech. Eng. Sci.* **2018**, *11*, 3917.

[33] W. Hao, J. Xie, F. Wang, Z. Liu, Z. Wang, *Int. J. Mech. Sci.* **2017**, *128–129*, 1.

[34] M. B. Azimi, M. Asgari, *Int. J. Mech. Sci.* **2016**, *105*, 253.

[35] S. Sinha, *Int. J. Eng. Sci. Invent.* **2017**, *9*, 7.

[36] W. Lee, Z. Tang, *Mater. Des.* **2014**, *58*, 116.

[37] Y. Xiang, M. Wang, *Int. J. Appl. Mech.* **2015**, *7*, 1550060.

[38] G. Lu, J. L. Yu, J. J. Zhang, T. X. Yu, *Int. J. Mech. Sci.* **2021**, *206*, 106610.

[39] T. Wierzbicki, W. Abramowicz, *J. Appl. Mech.* **1983**, *50*, 727.

[40] X. Zhang, H. Zhang, *Int. J. Impact Eng.* **2012**, *46*, 23.

[41] H. Yin, G. Wen, Z. Bai, Z. Chen, Q. Qing, *J. Sandwich Struct. Mater.* **2020**, *22*, 190.

[42] W. Johnson, P. D. Soden, S. T. S. Al-Hassani, *J. Strain Anal. Eng. Des.* **1977**, *12*, 317.